An inherently mass-conserving semi-implicit semi-Lagrangian discretisation of the shallow-water equations on the sphere

M. Zerroukat,[a]* N. Wood,[a] A. Staniforth,[a] A. A. White[a] and J. Thuburn[b]

[a]*Met Office, Exeter, UK* [†]
[b]*School of Engineering, Computing and Mathematics, University of Exeter, UK*

ABSTRACT: For the shallow-water equations on the sphere, an inherently mass-conserving semi-Lagrangian discretisation (SLICE) of the continuity equation is coupled with a semi-implicit semi-Lagrangian discretisation of the momentum equations. Various tests from the literature (two with analytical nonlinear solutions) are used to assess the model's performance and also to compare it with that of a variant model that instead employs a standard non-conserving semi-implicit semi-Lagrangian discretisation of the continuity equation. The mass-conserving version gives results that are overall somewhat better than the non-conserving one. Copyright © 2009 Royal Meteorological Society and Crown Copyright

1. Introduction

Because of their good performance at large timestep, Semi-Implicit Semi-Lagrangian (SISL) schemes are widely used for the dynamical cores of many operational numerical weather prediction (NWP) and climate models (Staniforth and Côté, 1991; Temperton *et al.*, 2001; Williamson, 2007). Arguably, the remaining drawback is the lack of inherent mass conservation, due to the intrinsically non-conservative nature of the interpolation used in such schemes. In practice, mass conservation is not a major problem in NWP due to the relatively short integration times. However, for climate simulations, lack of inherent mass conservation can cause a significant drift in the global mass (Moorthi *et al.*, 1995) and also introduce significant errors (Machenhauer and Olk, 1997). Lack of mass conservation has traditionally been dealt with by using *a posteriori* mass-fixing schemes, whereby global mass conservation is restored diagnostically, e.g. Priestley (1993) in the context of passive transport, and Gravel and Staniforth (1994) for a shallow-water model.

Significant progress has been made on developing semi-Lagrangian schemes that inherently conserve mass (Rančić, 1992, 1995; Nair and Machenhauer, 2002; Nair *et al.*, 2002, 2003, 2005; Zerroukat *et al.*, 2002, 2004, 2005, 2006, 2007, 2009; Mahidjiba *et al.*, 2008). This

has however been for the most part in the context of passive transport, rather than for the discretisation of coupled nonlinear fluid flow equations for which noise and stability are potential issues (Durran and Reinecke, 2004). An exception is the recent Lauritzen *et al.* (2006, 2008) work.

In Lauritzen *et al.* (2006), two locally mass-conserving Cell Integrated Semi-Lagrangian (CISL) schemes are applied to the continuity equation of a spherical limited-area SISL shallow-water equations (SWE) model. CISL results for a series of test cases are found to be similar to those of a SISL (non-conserving) version of their model. The stable application of the CISL schemes within the model is achieved in a somewhat complex manner in which the departure area requires explicit evaluation. (The complexity results from a desire to retain as much of the Lagrangian aspect of the implicit divergence term as possible, whilst simultaneously retaining as simple a Helmholtz equation as possible. These somewhat conflicting goals are reconciled via a predictor–corrector approach.) It is for this reason that the authors claim that the approach cannot be used with SLICE. (Our view is that this is incorrect since, whilst SLICE does not need any explicit knowledge of the departure areas, it could, with some expense, be used to evaluate these.) Additionally, parts of the Lauritzen *et al.* (2006) scheme use only first-order accurate trajectories, which can limit accuracy at large timestep (Staniforth and Pudykiewicz, 1985). Kaas (2008) follows a similar, but substantially simpler, route to couple his Locally Mass Conserving Semi-Lagrangian (LMCSL) scheme to a SISL Cartesian SWE model.

*Correspondence to: Mohamed Zerroukat, Met Office, FitzRoy Road, Exeter EX1 3PB, UK.

E-mail: Mohamed.Zerroukat@metoffice.gov.uk

Here SLICE is applied in a straightforward, yet stable, way to the continuity equation of a global SISL SWE model. Additionally, and importantly, the trajectories are evaluated to second-order accuracy.

The paper is organized as follows. The model is formulated in section 2; various tests from the literature are used in section 3 to illustrate the model's performance; and conclusions are drawn in section 4.

2. Formulation

2.1. The continuous equations

The SWEs can be written in (mass-conservative) Lagrangian form as

$$\frac{D\mathbf{u}}{Dt} = -2\Omega_r \times \mathbf{u} - \nabla \left(\Phi + \Phi^S \right) \equiv \Psi \,, \qquad (1)$$

$$\frac{D}{Dt}\left[\int_{\delta\mathcal{A}} \left(\Phi - \Phi^{\mathrm{ref}} \right) \mathrm{d}\mathcal{A} \right] = -\Phi^{\mathrm{ref}} \int_{\delta\mathcal{A}} \nabla \cdot \mathbf{u} \, \mathrm{d}\mathcal{A} \,, \qquad (2)$$

where $\mathbf{u}$ is the velocity vector; t is time; D/Dt is the total derivative following the fluid; Ω_r is a radial vector with magnitude given by the radial component of the Earth's rotation vector Ω; Φ is the geopotential of the free surface relative to the underlying rigid surface; Φ^S is the geopotential of this rigid surface relative to mean sea level; and Φ^{ref} is a constant, representative, reference value for Φ, introduced here in anticipation of a SISL discretisation. Also $\delta\mathcal{A}$ is a (finite) material area (this is an area, rather than a volume, as only two dimensions are considered here) that moves with the fluid. Equation (2) is the integral equivalent of the more usual form,

$$\frac{D}{Dt}\left(\Phi - \Phi^{\mathrm{ref}} \right) + \Phi^{\mathrm{ref}} \nabla \cdot \mathbf{u} = -\left(\Phi - \Phi^{\mathrm{ref}} \right) \nabla \cdot \mathbf{u} \,, \quad (3)$$

of the continuity equation used in traditional SISL discretisations.

The kinematic equation, also introduced in anticipation of a SISL discretisation, is

$$\frac{D\mathbf{x}}{Dt} = \mathbf{u}, \qquad (4)$$

where $\mathbf{x}$ is the position vector on the sphere relative to the centre of the sphere.

2.2. The SISL discrete equations in vector form

The continuous equations (1)–(2) and (4) are discretised in a SISL fashion as:

$$(\mathbf{u} - \alpha\Delta t\,\Psi)_A^{n+1} = (\mathbf{u} + \beta\,\Delta t\,\Psi)_D^n \,, \qquad (5)$$

$$\left\{ \int_{\delta\mathcal{A}} \left[\left(\Phi - \Phi^{\mathrm{ref}} \right) + \alpha\,\Delta t\,\Phi^{\mathrm{ref}} \nabla \cdot \mathbf{u} \right] \mathrm{d}\mathcal{A} \right\}_A^{n+1}$$
$$= \left\{ \int_{\delta\mathcal{A}} \left[\left(\Phi - \Phi^{\mathrm{ref}} \right) - \beta\,\Delta t\,\Phi^{\mathrm{ref}} \nabla \cdot \mathbf{u} \right] \mathrm{d}\mathcal{A} \right\}_D^n \,, \qquad (6)$$

$$(\mathbf{x} + \beta_x \Delta t\,\mathbf{u})_D^n = (\mathbf{x} - \alpha_x \Delta t\,\mathbf{u})_A^{n+1} \,, \qquad (7)$$

where α and α_x are the usual time weights; $\beta \equiv 1 - \alpha$; $\beta_x \equiv 1 - \alpha_x$; and Δt is the timestep size. Here subscripts A and D refer to evaluation at an arrival and departure point, respectively, or, for an integral quantity as in (6), at an arrival and departure cell, respectively. All the results presented here (see section 3) use the centred values $\alpha = \beta = \alpha_x = \beta_x = 1/2$, with associated second-order accuracy in time. The iterative approach to solving this set of implicit equations is outlined in Appendix D. This avoids the usual, and undesirable, extrapolation of nonlinear terms and of the wind field used in the trajectory calculation.

2.3. The SISL discrete equations in component form

Let (λ, ϕ) be the usual longitude–latitude spherical polar coordinates on a sphere of radius a, with velocity components

$$\mathbf{u} \equiv (u, v) \equiv \left(a\cos\phi\frac{D\lambda}{Dt}, a\frac{D\phi}{Dt} \right). \qquad (8)$$

The principal issue with writing the momentum equations in component form in spherical geometry is the evaluation of a vector field at the departure point, i.e. the right-hand side of (5). This is because, in spherical (and also other curvilinear) geometries, the unit basis vectors at the departure point are not in general aligned with those at the arrival point. In Staniforth *et al.* (2009) it is shown how to address this issue by defining a rotation matrix Λ whose elements depend on the unit basis vectors at both the departure and the arrival points.

Using this approach (with a slight abuse of vector notation), (5) becomes

$$(\mathbf{u} - \alpha\Delta t\Psi)_A^{n+1} = \left[\Lambda\,(\mathbf{u} + \beta\,\Delta t\,\Psi)_{D_L}^n \right], \qquad (9)$$

where subscript D_L denotes evaluation at the departure point in terms of the local basis vectors at that departure point (the usual subscript D also denotes evaluation of the departure point, but instead in terms of the basis vectors of the arrival point). The elements of the rotation matrix Λ are given explicitly in appendix A.

Taking the components of (9) with respect to the unit vectors at the arrival point then leads to

$$(u - \alpha\Delta t\,\Psi_u)_A^{n+1} = \Lambda_{11}\,(u + \beta\,\Delta t\,\Psi_u)_{D_L}^n$$
$$+ \Lambda_{12}\,(v + \beta\,\Delta t\,\Psi_v)_{D_L}^n \,, \qquad (10)$$

$$(v - \alpha\Delta t\,\Psi_v)_A^{n+1} = \Lambda_{21}\,(u + \beta\,\Delta t\,\Psi_u)_{D_L}^n$$
$$+ \Lambda_{22}\,(v + \beta\,\Delta t\,\Psi_v)_{D_L}^n \,, \qquad (11)$$

where

$$\Psi_u \equiv -2\,(\Omega_r \times \mathbf{u})_u - \frac{1}{a\cos\phi}\frac{\partial}{\partial\lambda}\left(\Phi + \Phi^S \right), \qquad (12)$$

$$\Psi_v \equiv -2\,(\Omega_r \times \mathbf{u})_v - \frac{1}{a}\frac{\partial}{\partial\phi}\left(\Phi + \Phi^S \right). \qquad (13)$$

Being a scalar equation, the continuity equation (6) remains unchanged.

The departure point equation (7) for $\mathbf{x}_D^n$ is solved iteratively using a local Cartesian transform approach – see Appendix B for a summary of this procedure, and Wood *et al.* (2009) for a detailed derivation. Unlike traditional two-time-level semi-Lagrangian schemes, the present departure calculations do not use any extrapolated wind. As summarised in Appendix D, the wind at level n and the latest update at $(n + 1)$ are used within an iterative framework.

2.4. Spatial discretisation

The spatial discretisation follows closely one of the schemes derived in Thuburn and Staniforth (2004), here-inafter referred to as TS04. Dependent variables are staggered with respect to one another on an Arakawa C grid and, as recommended in TS04, v is placed at the poles in preference to u and Φ. The discretisation employs two-point differencing and averaging operators – see Appendix C for their definitions – and, as noted in TS04, it can be equivalently viewed as being based on either finite differences or finite volumes. Our preference is the finite-volume viewpoint, consistent with the finite-volume basis for the SLICE transport scheme used herein.

After spatial discretisation, (10)–(11) become

$$(u - \alpha \Delta t \Psi_u)_A^{n+1} = \Lambda_{11} (u + \beta \Delta t \Psi_u)_{D_L^u}^n$$
$$+ \Lambda_{12} (v + \beta \Delta t \Psi_v)_{D_L^u}^n$$
$$\equiv R_u^n, \qquad (14)$$

$$(v - \alpha \Delta t \Psi_v)_A^{n+1} = \Lambda_{21} (u + \beta \Delta t \Psi_u)_{D_L^v}^n$$
$$+ \Lambda_{22} (v + \beta \Delta t \Psi_v)_{D_L^v}^n$$
$$\equiv R_v^n, \qquad (15)$$

where the superscripts on D_L indicate the gridpoint whose departure point is to be used, and (12) and (13) are redefined as

$$\Psi_u \equiv -2 (\Omega_r \times \mathbf{u})_u - \frac{1}{a \cos \phi} \delta_\lambda (\Phi + \Phi^S), \qquad (16)$$

$$\Psi_v \equiv -2 (\Omega_r \times \mathbf{u})_v - \frac{1}{a} \delta_\phi (\Phi + \Phi^S), \qquad (17)$$

where the difference operators δ_λ and δ_ϕ are defined in Appendix C.

The Coriolis terms in (16)–(17) are evaluated following TS04. As shown therein, this leads, for the linearised equations with v placed at the poles, to good Rossby mode dispersion properties, and also ensures that the Coriolis terms provide no source or sink of energy. Thus

$$-2 (\Omega_r \times \mathbf{u})_u = \frac{1}{a \cos \phi \Delta \lambda} \left\langle \overline{\tilde{v}}^\phi \frac{f}{\Phi} \right\rangle^\lambda, \qquad (18)$$

$$-2 (\Omega_r \times \mathbf{u})_v = -\frac{1}{a \Delta \phi} \left\langle \overline{\tilde{u}}^\lambda \frac{f}{\Phi} \right\rangle^\phi, \qquad (19)$$

where

$$\tilde{u} \equiv a \Delta \phi \, \overline{\Phi}^\lambda u, \qquad (20)$$

$$\tilde{v} \equiv a \cos \phi \Delta \lambda \, \overline{\Phi}^\phi v, \qquad (21)$$

are mass flux variables (cf. Equations (2.6)–(2.7) of TS04),

$$f \equiv 2\Omega \sin \phi \qquad (22)$$

is assumed to be evaluated and stored at Φ points (as suggested by Thuburn, 2007, for good Rossby mode dispersion on a C-grid), $\Omega = |\Omega|$ is the magnitude of the Earth's rotation vector, and the averaging operators, $\langle \cdot \rangle$ and $\overline{(\cdot)}$, are defined in Appendix C.

The discrete continuity equation (6) can be rewritten as

$$\left[(\Phi - \Phi^{\text{ref}}) + \alpha \Delta t \, \Phi^{\text{ref}} \nabla \cdot \mathbf{u} \right]_A^{n+1} = R_\Phi^n, \qquad (23)$$

where the integral term

$$R_\Phi^n \equiv \frac{1}{\Delta \mathcal{A}} \left\{ \iint_{\delta \mathcal{A}} \left[(\Phi - \Phi^{\text{ref}}) - \beta \Delta t \, \Phi^{\text{ref}} \nabla \cdot \mathbf{u} \right] d\mathcal{A} \right\}_D^n, \qquad (24)$$

is computed using the C-SLICE conservative remapping algorithm (Zerroukat *et al.*, 2009), and $\Delta \mathcal{A} \equiv a^2 \cos \phi \Delta \lambda \Delta \phi$ is the discrete element of area of the arrival cell. Also, the divergence term is computed as

$$\nabla \cdot \mathbf{u}_A^{n+1} = \frac{1}{a \cos \phi} \left[\delta_\lambda u + \delta_\phi (v \cos \phi) \right]_A^{n+1}. \qquad (25)$$

2.5. The Helmholtz equation

With the definitions

$$u' \equiv u_A^{n+1}, \quad v' \equiv v_A^{n+1}, \quad \Phi' \equiv \Phi_A^{n+1} - \Phi^{\text{ref}}, \qquad (26)$$

the momentum equations (14)–(15), and the continuity equation (23), can be rewritten as

$$u' + H_u \delta_\lambda \Phi' = R_u^* + R_u^n, \qquad (27)$$
$$v' + H_v \delta_\phi \Phi' = R_v^* + R_v^n, \qquad (28)$$
$$\Phi' + H_\Phi \left[\delta_\lambda (H_\lambda u') + \delta_\phi (H_\phi v') \right] = R_\Phi^n, \qquad (29)$$

where

$$R_u^* \equiv \alpha \Delta t \left[-2 (\Omega_r \times \mathbf{u})_u - \frac{1}{a \cos \phi} \delta_\lambda \Phi^S \right]_A^{n+1}, \qquad (30)$$

$$R_v^* \equiv \alpha \Delta t \left[-2 (\Omega_r \times \mathbf{u})_v - \frac{1}{a} \delta_\phi \Phi^S \right]_A^{n+1}, \qquad (31)$$

$$H_u \equiv \frac{\alpha \Delta t}{a \cos \phi}, \quad H_v \equiv \frac{\alpha \Delta t}{a}, \qquad (32)$$

$$H_\lambda \equiv a \Phi^{\text{ref}}, \ H_\phi \equiv a \cos \phi \, \Phi^{\text{ref}}, \ H_\Phi \equiv \frac{\alpha \Delta t}{a^2 \cos \phi}. \qquad (33)$$

Algebraically eliminating u' and v' from (27)–(29) then leads to the Helmholtz problem

$$H_\Phi \delta_\lambda \left[H_\lambda \left(H_u \delta_\lambda \Phi' \right) \right] + H_\Phi \delta_\phi \left[H_\phi \left(H_v \delta_\phi \Phi' \right) \right] - \Phi'$$
$$= \Re^* + \Re^n, \tag{34}$$

where $\qquad \Re^* \equiv \mathscr{D}\left(R_u^*, R_v^* \right), \tag{35}$

$$\Re^n \equiv \mathscr{D}\left(R_u^n, R_v^n \right) - R_\Phi^n, \tag{36}$$

$$\mathscr{D}\left(F, G \right) \equiv H_\Phi \left[\delta_\lambda \left(H_\lambda F \right) + \delta_\phi \left(H_\phi G \right) \right]. \tag{37}$$

The coefficients on the left-hand side of (34) (i.e. the H's) are independent of time. The right-hand side of (34) contains both an explicitly known term (i.e. $\Re^n$) and an implicitly defined nonlinear term (i.e. $\Re^*$), leading to a nonlinear coupling with (27)–(28).

The nonlinear set of coupled equations (27), (28) and (34) are solved using an iterative approach (Appendix D provides details). Since the Coriolis terms are handled iteratively, i.e. they appear on the right-hand side of (27) and (28), convergence of the iterative procedure requires that $\Omega \Delta t / 2 \le 1$.

2.6. Standard SISL version of the model

To facilitate validation of the model, a version has been created that differs only in its use of a standard SISL discretisation of the continuity equation, i.e. the discretisation (23) of (2) is replaced by the discretisation

$$\left[\left(\Phi - \Phi^{\text{ref}} \right) + \alpha \, \Delta t \, \Phi^{\text{ref}} \nabla \cdot \mathbf{u} \right]_A^{n+1} = R_\Phi^* + R_\Phi^n, \tag{38}$$

of (3), where

$$R_\Phi^* \equiv -\alpha \, \Delta t \left[\left(\Phi - \Phi^{\text{ref}} \right) \nabla \cdot \mathbf{u} \right]_A^{n+1}, \tag{39}$$

and now

$$R_\Phi^n \equiv \left[\left(\Phi - \Phi^{\text{ref}} \right) - \beta \, \Delta t \, \Phi \nabla \cdot \mathbf{u} \right]_D^n. \tag{40}$$

Since (38) has the same form as (23), except for the addition of the term R_Φ^*, the solution procedure described above goes through virtually unchanged. The only real difference in the procedure is that the $\Re^*$ term in (34) has an additional contribution, $-R_\Phi^*$, which is evaluated in the inner loop when $\mathscr{D}\left(R_u^*, R_v^* \right)$ is evaluated. The resulting version of the model corresponds to a standard two-time-level fully interpolating (i.e. no time extrapolation) SISL discretisation of the shallow-water equations.

3. Computational examples

3.1. Preliminaries

Sample results for three test problems are presented below, with initial conditions obtained by evaluating analytically specified ones at gridpoints. The three test problems are integrated using various timesteps Δt on various grid resolutions $I \times J$ (I and J are the number of control-volumes in the λ and ϕ directions, respectively).

For all experiments, the physical constants a (mean Earth radius), Ω (Earth's rotation rate), and g (acceleration due to gravity) are set to the values given in Williamson *et al.* (1992): thus $a = 6.37122 \times 10^6$ m, $\Omega = 7.292 \times 10^{-5}$ s^{-1}, and $g = 9.80616$ m s^{-2}.

Recall (see algorithm of Appendix D) that L and M are the number of inner and outer iterations, respectively. For all results presented here, $L = M = 2$. Additionally: the time weights are all set to one half, i.e. $\alpha = \beta = \alpha_x = \beta_x = 1/2$, so the scheme is centred and second-order accurate in time; and Φ^{ref} is set to the minimax value of the initial Φ field, i.e. to $\Phi^{\text{ref}} = \{\min\left(\Phi|_{t=0} \right) + \max\left(\Phi|_{t=0} \right)\} / 2$.

3.2. Stationary jets over a zonal orography

This test is based on the exact axisymmetric stationary twin-jet solution, described in detail in section 2.3.2 of Staniforth and White (2007), viz.

$$u\left(\phi \right) = 4u_{\max} \cos \phi \left(1 - \cos \phi \right), \tag{41}$$
$$v = 0, \tag{42}$$

$$\Phi\left(\phi \right) = \Phi_0 + 8u_{\max}^2 \cos^2 \phi \left(1 - \frac{4\cos\phi}{3} + \frac{\cos^2\phi}{2} \right)$$
$$+ 4\Omega \, a \, u_{\max} \cos^2 \phi \left(1 - \frac{2\cos\phi}{3} \right) - \Phi^{\text{S}}(\phi), \tag{43}$$

with the parameters set to $u_{\max} = 50$ m s^{-1} and $\Phi_0 = 10^5$ m^2 s^{-2}. The orography is arbitrarily chosen to be a cosine-squared hill such that

$$\Phi^{\text{S}}(\phi) = \Phi_0^{\text{S}} \cos^2 \left[\frac{\pi}{W}(\phi - \phi_c) \right] \quad \text{for } |\phi - \phi_c| \le \frac{W}{2},$$
$$= 0 \text{ otherwise}, \tag{44}$$

where the maximum surface orographic height $\Phi_0^{\text{S}}/g = 3 \times 10^3$ m, its latitudinal width $W = \pi/3$, and the hill is centred at $\phi = \phi_c = \pi/4$.

(In the absence of orography, Staniforth and White (2008a) have shown that this solution is guaranteed to be physically stable when subjected to small but otherwise arbitrary perturbations: this ensures that any significant time evolution observed in a numerical solution must be of numerical origin, and not due to an inherent physical instability of the flow. Stability of the solution in the presence of the orography (44) has recently been demonstrated by White and Staniforth (2009).)

The exact solution described above is, however, essentially one-dimensional since it only depends upon ϕ, and not upon λ. To construct a numerically more challenging test case, Staniforth and White (2007) suggest defining the solution in a rotated (λ', ϕ') coordinate system, using the procedure given in their appendix, to obtain a test problem that varies two-dimensionally in the rotated coordinate system. This approach is adopted here with the model's polar axis inclined at an angle $\alpha_{\text{axis}} = \pi/6$ with respect to the geographical one. (Note that the Coriolis terms in the model, which uses the (λ', ϕ') coordinate system, have to be modified to depend upon
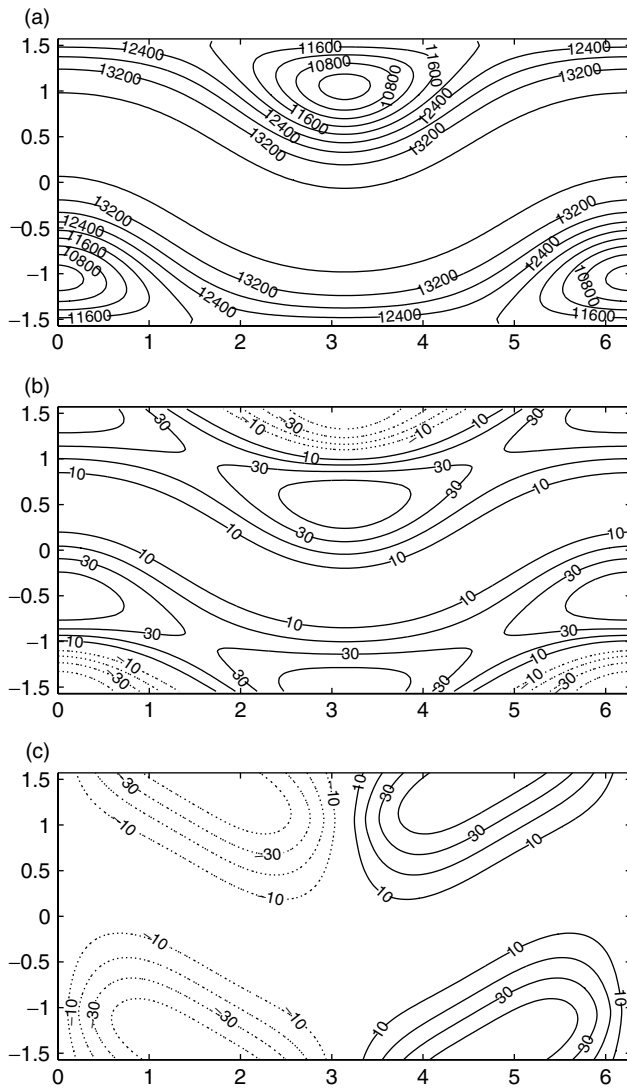
Figure 1. Initial fields for the stationary jets problem: (a) $\left(\Phi + \Phi^S\right)/g$, (b) u, and (c) v. The contour intervals are $400\,\text{m}$ for $\left(\Phi + \Phi^S\right)/g$, and $10\,\text{m}\,\text{s}^{-1}$ for u and v; solid lines denote positive contours, dashed lines negative contours, and there is no zero contour.
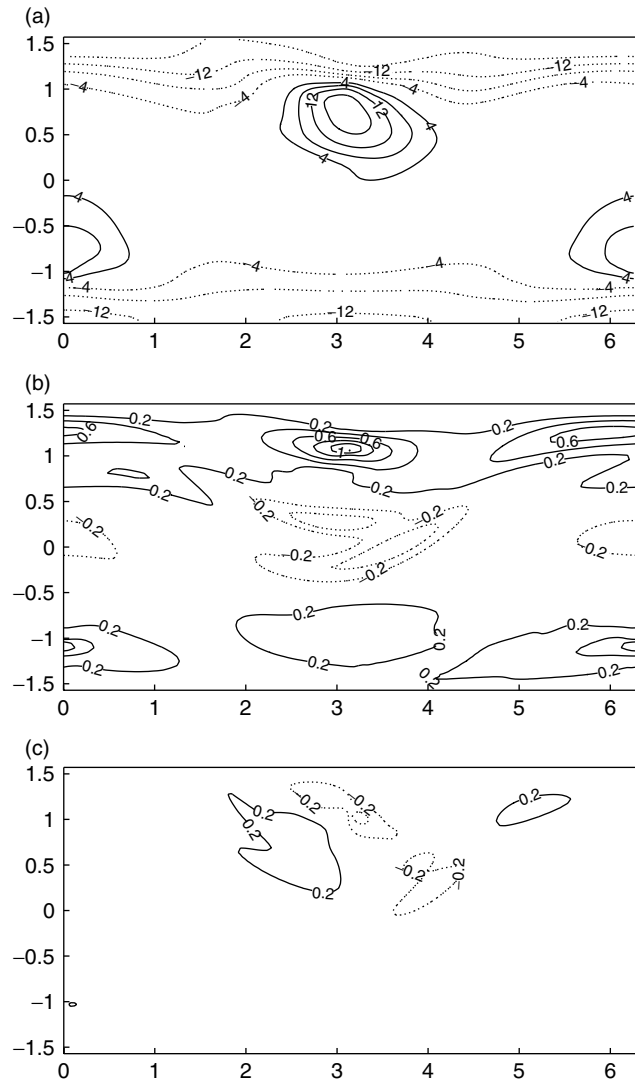

Figure 2. As Figure 1, but showing the error fields (numerical minus exact) after 5 days of integration using the mass-conserving model. $I = 128$, $J = 64$, $L = M = 2$, and $\triangle t = 1$ hour. Contour intervals are $4\,\text{m}$ for $\left(\Phi + \Phi^S\right)/g$, and $0.2\,\text{m}\,\text{s}^{-1}$ for u and v.

both λ' and ϕ', rather than on just the single variable ϕ in the unrotated coordinate system.) The initial fields for $\left(\Phi + \Phi^S\right)/g$, u and v are displayed in Figure 1 over the domain of integration.

Both the mass-conserving and standard SISL models have been integrated on 64×32, 128×64 and 256×128 uniform longitude–latitude grids to 5 days with Δt chosen so that the meridional Courant number based on $u_{\max}$, $C \equiv u_{\max}\Delta t /\left(a\Delta\phi\right)$, is identical for all the integrations, i.e. $C \approx 0.576$. It is worth noting that the zonal Courant number, $C_\lambda \equiv u_{\max}\Delta t /\left(a\Delta\lambda\cos\phi\right)$, differs, on a uniform longitude–latitude grid, from C by a factor $1/\cos\phi$. For the u-points nearest to the pole, this factor is $1/\sin\left(\Delta\phi/2\right)$, giving an increase compared with C of a factor of approximately 20, 40 and 80, respectively, for the 64×32, 128×64 and 256×128 grids.

As a sample result, the error fields (forecast minus exact) at 5 days for $\left(\Phi + \Phi^S\right)/g$, u and v for one of these integrations, viz. the mass-conserving one on the

128×64 grid, are shown in Figure 2. The errors are quite small in magnitude – plots of the forecast fields are visually indistinguishable from those of the corresponding exact ones. Although the analytic solution is in exact, stationary, balance, the model's numerics do not, in general, exactly represent this balance when using initial conditions obtained by evaluating the exact solution on the model's grid. A numerical adjustment process, akin to geostrophic adjustment, thus takes place in response to this small imbalance at initial time. Although the $\left(\Phi + \Phi^S\right)/g$, u and v fields of the exact solution in the Northern and Southern Hemispheres all exhibit certain symmetry/antisymmetry properties, the analogous numerical forecast fields (and therefore also the error fields) do not. This is because the orography field Φ^S, as specified in the unrotated coordinates by (44), does not possess a hemispheric symmetry/antisymmetry property – it is non-zero in one hemisphere and identically zero in the other – and consequently neither does the

Φ field. Analytically this does not adversely affect the symmetry/antisymmetry properties of the $\left(\Phi + \Phi^S\right)/g$, u and v fields. It does however change how the force balance is achieved: over orography, the gradient of orography provides part of the pressure gradient force needed in the absence of orography. Numerically, however, this is only approximately achieved, resulting in larger errors over and near orography, and a consequent loss of symmetry/antisymmetry in the $\left(\Phi + \Phi^S\right)/g$, u and v forecast and error fields, as seen in the error fields of Figure 2.

The l_1, l_2 and l_∞ error norms for $h \equiv \left(\Phi + \Phi^S\right)/g$ and $\mathbf{v}$, as defined in Williamson *et al.* (1992), have been computed at 5 days for all of the above-mentioned integrations. These are displayed in Tables I and II for the mass-conserving and standard SISL integrations, respectively. Examination of these tables shows that the error measures of the mass-conserving model are, without exception, somewhat smaller than those of the standard SISL model. This can be attributed to the enhanced accuracy of the Parabolic Spline Method, used within C-SLICE to conservatively remap mass in the mass-conserving model, compared with cubic-Lagrange interpolation, used to (non-conservatively) transport mass in the standard SISL model. Also, the error measures for both models diminish approximately quadratically as the grid length and timestep are simultaneously halved, consistent with the use of second-order-accurate centred time and space differencing.

3.3. Exact unsteady flow

Läuter *et al.* (2005) have recently derived time-dependent closed-form exact solutions of the SWEs. Unlike most exact solutions for tests used in the past (which are mostly independent of time), these solutions are a major step forward in testing and validating numerical shallow-water models, as they facilitate quantitative assessment of the time-dependent aspects. (Staniforth and White (2008b) generalised this derivation to three dimensions in spherical geometry thereby further extending the usefulness of the approach beyond the SWEs.) Läuter *et al.* (2005) have shown that the following is an exact solution of the SWEs:

$$u(\lambda, \phi, t)$$
$$= u_0 \left\{ \sin\alpha_{\text{axis}} \sin\phi \cos(\lambda + \Omega t) + \cos\alpha_{\text{axis}} \cos\phi \right\}, \quad (45)$$

$$v(\lambda, t) = -u_0 \sin\alpha_{\text{axis}} \sin(\lambda + \Omega t), \quad (46)$$

$$\Phi(\lambda, \phi, t) =$$
$$\Phi_0 - \frac{1}{2}\{u_0 \left[\cos\alpha_{\text{axis}} \sin\phi - \sin\alpha_{\text{axis}} \cos\phi \cos(\lambda + \Omega t)\right]$$
$$+ a\,\Omega \sin\phi\}^2, \quad (47)$$

$$\Phi^S(\lambda, \phi) = \frac{1}{2}\left(a\,\Omega \sin\phi\right)^2. \quad (48)$$

Following Läuter *et al.* (2005, 2007), the following parameter values are used: $u_0 = 2\pi a/12$ m day^{-1}, $\Phi_0 = 133\,681$ m^2 s^{-2}, and $\alpha_{\text{axis}} = \pi/4$. The initial fields for $\left(\Phi + \Phi^S\right)/g$, u and v are displayed in Figure 3 over the domain of integration. Because the exact solution is periodic with the diurnal frequency Ω, the initial fields also correspond to the exact solution an integer number of days later.

Both the mass-conserving and standard SISL models have been integrated on 64×32, 128×64 and 256×128 uniform longitude–latitude grids to 5 days. The timesteps have been chosen to give one of two values for the u_0-based meridional Courant number $C \equiv u_0 \Delta t / (a \Delta \phi)$; viz. $C_{\text{small}} \approx 0.092$ and $C_{\text{large}} \equiv 10 C_{\text{small}} \approx 0.92$. The value of C_{small} has been chosen to be approximately the same as that used by Läuter *et al.* (2007) for a similar set of experiments, run at various resolutions at a constant Courant number, which they give as $C_L \equiv u\,900$ s$/854$ km ≈ 0.0843, using their PLASMA model on a global triangular grid. The value of C_{large} corresponds to adopting the same set of timesteps used to produce the results for the stationary jets test case described above. As for that case, the corresponding zonal Courant number, $C_\lambda \equiv u_0 \Delta t / (a \Delta \lambda \cos \phi)$, at

Table I. Error norms after 5 days of integration at various resolutions for the midlatitude jets problem using the mass-conserving model. Δt in minutes.

$I \times J$	Δt	$l_1(h)$	$l_2(h)$	$l_\infty(h)$	$l_1(\mathbf{v})$	$l_2(\mathbf{v})$	$l_\infty(\mathbf{v})$
64×32	120	0.101×10^{-2}	0.165×10^{-2}	0.583×10^{-2}	0.341×10^{-1}	0.333×10^{-1}	0.820×10^{-1}
128×64	60	0.258×10^{-3}	0.406×10^{-3}	0.141×10^{-2}	0.859×10^{-2}	0.839×10^{-2}	0.245×10^{-1}
256×128	30	0.634×10^{-4}	0.989×10^{-4}	0.326×10^{-3}	0.214×10^{-2}	0.208×10^{-2}	0.646×10^{-2}

Table II. As Table I, but using the standard SISL model.

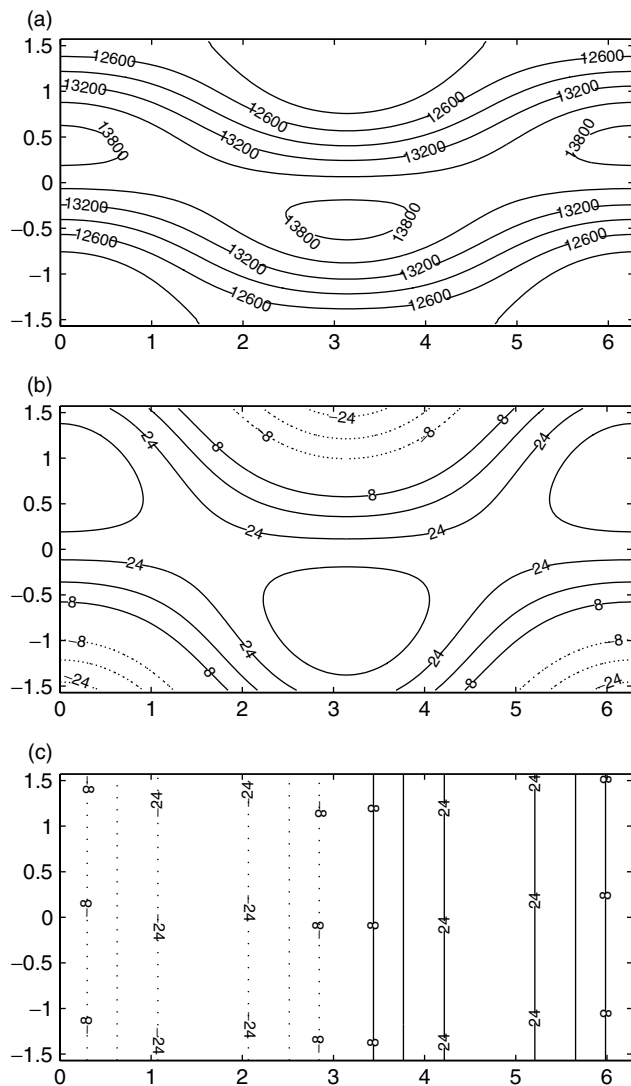| $I \times J$	Δt	$l_1(h)$	$l_2(h)$	$l_\infty(h)$	$l_1(\mathbf{v})$	$l_2(\mathbf{v})$	$l_\infty(\mathbf{v})$
64×32	120	0.109×10^{-2}	0.178×10^{-2}	0.657×10^{-2}	0.365×10^{-1}	0.363×10^{-1}	0.915×10^{-1}
128×64	60	0.288×10^{-3}	0.464×10^{-3}	0.171×10^{-2}	0.941×10^{-2}	0.946×10^{-2}	0.266×10^{-1}
256×128	30	0.709×10^{-4}	0.116×10^{-3}	0.417×10^{-3}	0.237×10^{-2}	0.238×10^{-2}	0.730×10^{-2}

Figure 3. Initial fields for the exact unsteady flow problem: (a) $\left(\Phi + \Phi^S\right)/g$; (b) u; (c) v. Contour intervals are $400\,\text{m}$ for $\left(\Phi + \Phi^S\right)/g$, and $10\,\text{m s}^{-1}$ for u and v; solid lines denote positive contours, dashed lines negative contours, and there is no zero contour.
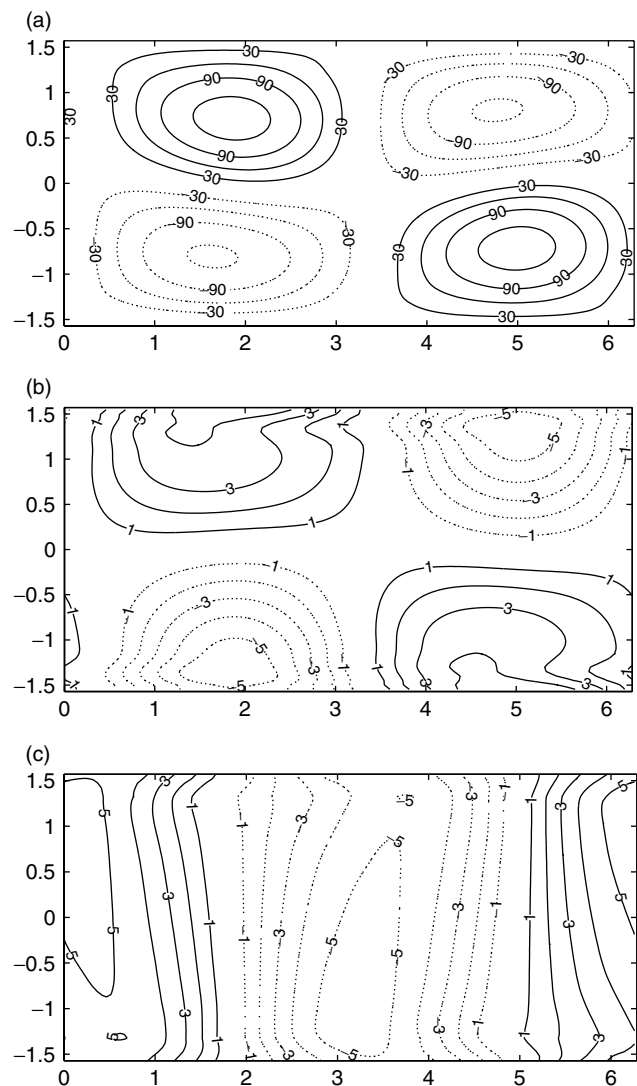

Figure 4. As Figure 3, but showing the error fields (numerical minus exact) after 5 days of integration using the mass-conserving model. $I = 128$, $J = 64$, $L = M = 2$, and $\triangle t = 1\,\text{hour}$. Contour intervals are $30\,\text{m}$ for $\left(\Phi + \Phi^S\right)/g$, and $1\,\text{m s}^{-1}$ for u and v.

the rows nearest to the poles, is larger than C by a factor of approximately 20, 40 and 80, respectively, for the 64×32, 128×64 and 256×128 resolutions.

As a sample result, the error fields (forecast minus exact) at 5 days for $\left(\Phi + \Phi^S\right)/g$, u and v for one of the integrations, viz. the mass-conserving one on the 128×64 grid, are shown in Figure 4. Note that the initial symmetry/antisymmetry properties between the Northern and Southern Hemispheres are preserved in the forecast fields (and therefore also in the error fields). Examination of overlays (not shown) of the forecast and exact fields reveals that the errors are primarily due to a small east–west phase lag in the numerical solution of approximately 1.3 degrees of longitude per day, with negligible distortion and numerical damping.

The l_1, l_2 and l_∞ error norms for $\left(\Phi + \Phi^S\right)/g$ and **v** of the above-mentioned integrations have also been computed at 5 days. They are displayed for $C_{\text{small}} \approx 0.092$ in Tables III–IV for the mass-conserving and standard

SISL integrations, respectively, and correspondingly in Tables V–VI for $C_{\text{large}} \approx 0.92$. (Error norms for integrations using an extra, low-resolution, 32×16 grid have also been included in Tables III–IV to facilitate comparison with the results presented in Läuter *et al.* (2007).) Examination of Tables III–VI shows that the l_1 and l_2 error norms of the mass-conserving model are mostly a little smaller than those of the standard SISL model, particularly at long timestep. Also, the error norms diminish approximately quadratically as the grid length and timestep are simultaneously halved, again consistent with the use of second-order-accurate centred time and space differencing.

The C_{small} (≈ 0.092) l_2 error norms for the mass-conserving and standard SISL models, displayed in Tables III–IV, respectively, may be compared with those shown graphically in the right-hand panel of Figure 3 of Läuter *et al.* (2007) for their PLASMA model integrated on a global triangular grid. It is seen that the l_2 error

Table III. Error norms after 5 days of integration at various resolutions for the exact unsteady problem using the mass-conserving model; Δt in minutes.

$I \times J$	Δt	$l_1(h)$	$l_2(h)$	$l_\infty(h)$	$l_1(\mathbf{v})$	$l_2(\mathbf{v})$	$l_\infty(\mathbf{v})$
32×16	24	0.458×10^{-2}	0.553×10^{-2}	0.111×10^{-1}	0.143×10^{0}	0.150×10^{0}	0.390×10^{0}
64×32	12	0.142×10^{-2}	0.176×10^{-2}	0.348×10^{-2}	0.408×10^{-1}	0.428×10^{-1}	0.136×10^{0}
128×64	6	0.357×10^{-3}	0.447×10^{-3}	0.888×10^{-3}	0.109×10^{-1}	0.114×10^{-1}	0.425×10^{-1}
256×128	3	0.894×10^{-4}	0.113×10^{-3}	0.228×10^{-3}	0.279×10^{-2}	0.289×10^{-2}	0.101×10^{-1}

Table IV. As Table III, but for the standard SISL model.

$I \times J$	Δt	$l_1(h)$	$l_2(h)$	$l_\infty(h)$	$l_1(\mathbf{v})$	$l_2(\mathbf{v})$	$l_\infty(\mathbf{v})$
32×16	24	0.518×10^{-2}	0.613×10^{-2}	0.122×10^{-1}	0.144×10^{0}	0.151×10^{0}	0.344×10^{0}
64×32	12	0.147×10^{-2}	0.179×10^{-2}	0.355×10^{-2}	0.410×10^{-1}	0.429×10^{-1}	0.138×10^{0}
128×64	6	0.362×10^{-3}	0.447×10^{-3}	0.878×10^{-3}	0.108×10^{-1}	0.114×10^{-1}	0.426×10^{-1}
256×128	3	0.896×10^{-4}	0.111×10^{-3}	0.217×10^{-3}	0.273×10^{-2}	0.285×10^{-2}	0.104×10^{-1}

Table V. As Table III, but for a ten times longer timestep.

$I \times J$	Δt	$l_1(h)$	$l_2(h)$	$l_\infty(h)$	$l_1(\mathbf{v})$	$l_2(\mathbf{v})$	$l_\infty(\mathbf{v})$
64×32	120	0.162×10^{-1}	0.196×10^{-1}	0.377×10^{-1}	0.536×10^{0}	0.536×10^{0}	0.549×10^{0}
128×64	60	0.420×10^{-2}	0.507×10^{-2}	0.963×10^{-2}	0.135×10^{0}	0.135×10^{0}	0.157×10^{0}
256×128	30	0.102×10^{-2}	0.123×10^{-2}	0.231×10^{-2}	0.324×10^{-1}	0.325×10^{-1}	0.522×10^{-1}

Table VI. As Table V, but for the standard SISL model.

$I \times J$	Δt	$l_1(h)$	$l_2(h)$	$l_\infty(h)$	$l_1(\mathbf{v})$	$l_2(\mathbf{v})$	$l_\infty(\mathbf{v})$
64×32	120	0.165×10^{-1}	0.201×10^{-1}	0.393×10^{-1}	0.543×10^{0}	0.542×10^{0}	0.557×10^{0}
128×64	60	0.423×10^{-2}	0.510×10^{-2}	0.942×10^{-2}	0.136×10^{0}	0.136×10^{0}	0.143×10^{0}
256×128	30	0.102×10^{-2}	0.123×10^{-2}	0.229×10^{-2}	0.329×10^{-1}	0.329×10^{-1}	0.361×10^{-1}

norms of the mass-conserving and standard SISL models are significantly smaller than the corresponding ones for the PLASMA model, and this is particularly so at high resolution. For example, the PLASMA model with grid lengths of 1041 km and 261 km gives l_2 error norms of approximately 20×10^{-3} and 8×10^{-3}, respectively, whereas the mass-conserving model with the somewhat coarser grid lengths of 1250 km and 312 km gives l_2 error norms of 5.6×10^{-3} and 0.45×10^{-3}, respectively.

3.4. Zonal flow over an isolated mountain

This is test case 5 of Williamson *et al.* (1992), an initially zonal flow impinging on an isolated conically shaped mountain; it has no known exact solution. The initial conditions are

$$u(\phi) = u_0 \cos \phi, \qquad (49)$$
$$v = 0, \qquad (50)$$
$$\Phi(\phi) = \Phi_0 - \left(a \, \Omega + \frac{u_0}{2}\right) u_0 \sin^2 \phi, \qquad (51)$$

where $u_0 = 20 \, \mathrm{m \, s^{-1}}$; $\Phi_0/g = 5\,960$ m. The orography is defined such that $\Phi^S = \Phi_0^S (1 - r/R)$, where $r^2 = \min \left\{ R^2, (\lambda - \lambda_c)^2 + (\phi - \phi_c)^2 \right\}$: the maximum height of the mountain is $\Phi_0^S/g = 2\,000$ m; the centre of the mountain is located at $(\lambda_c, \phi_c) = (3\pi/2, \pi/6)$; and $R = \pi/9$ defines the horizontal scale of the mountain.

The mass-conserving model was integrated on a 128×64 uniform longitude–latitude grid, first using a timestep of length $\Delta t = 600$ s, as in Lin and Rood (1997), and then with a 10-times larger timestep $\Delta t = 6\,000$ s. Results after 5 and 15 days are displayed in Figures 5–7 for the total height field $(\Phi + \Phi^S)/g$, the zonal wind component u, and the meridional wind component v, respectively. In each of these figures, results with a 600 s timestep are displayed after 5 and 15 days in panels (a) and (b), respectively: the corresponding result at 15 days with a 10-times larger timestep of 6 000 s is then displayed in panel (c).

For each of these three figures, by comparing (b) with (c), it is seen that the results using a 10-times longer

(a)

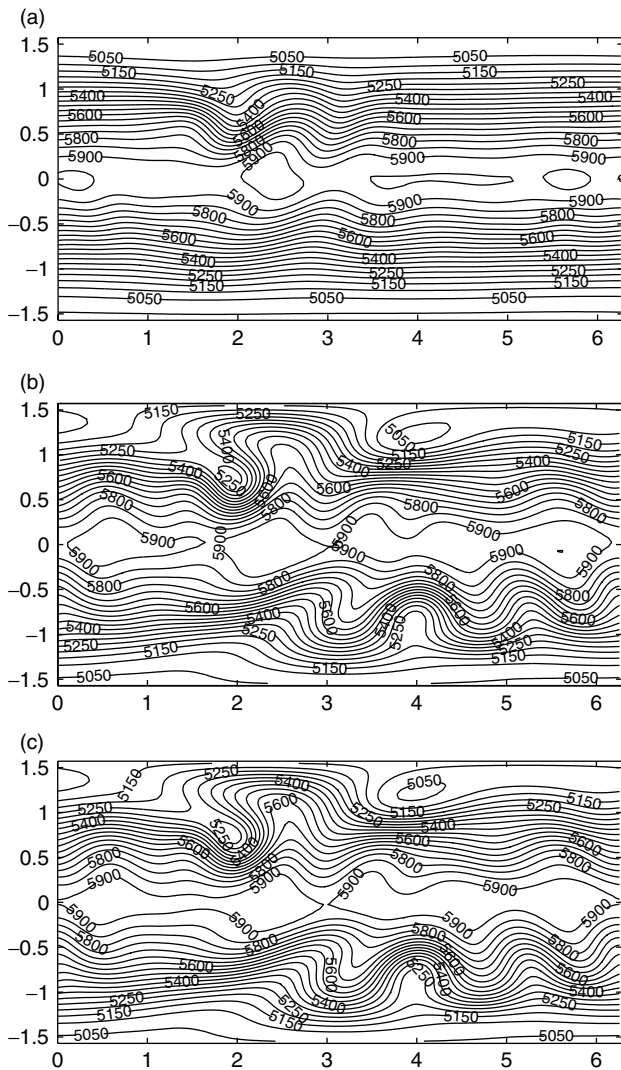

(a)

(b)

(b)

(c)

(c)

Figure 5. Total height field $(\Phi + \Phi^S)/g$ (m) of the numerical solution using the mass-conserving model for zonal flow over an isolated mountain on a 128×64 ($I \times J$) grid after (a) 5 days with $\triangle t = 600$ s, (b) 15 days with $\triangle t = 600$ s and (c) 15 days with $\triangle t = 6\,000$ s. The contour interval is 50 m.

Figure 6. As Figure 5, but for the zonal wind component u. The contour interval is $5\,\mathrm{m\,s^{-1}}$; solid lines denote positive contours, dashed lines negative contours, and there is no zero contour.

timestep ($6\,000$ s versus 600 s) are almost indistinguishable from those with the shorter timestep, albeit with a small difference at the Tropics.

The standard SISL model has also been integrated for this test case with the longer, $6\,000$ s, timestep, and the results after 15 days of integration are displayed in Figure 8. Comparing (a), (b) and (c) of this figure with Figures 5(c), 6(c) and 7(c), respectively, for the corresponding integration using the mass-conserving model, it is seen that the results of both models with the longer, $6\,000$ s, timestep are also almost indistinguishable.

For this test case, Lin and Rood (1997) integrated their explicit flux-form semi-Lagrangian shallow-water model at the same 128×64 spatial resolution using a 600 s timestep; their timestep is limited by a stability condition imposed by the use of a forward–backward scheme to discretise the terms responsible for gravity-wave propagation. Comparison of their Figures 4(a), 5(a) and 6(a) with the corresponding results displayed in our
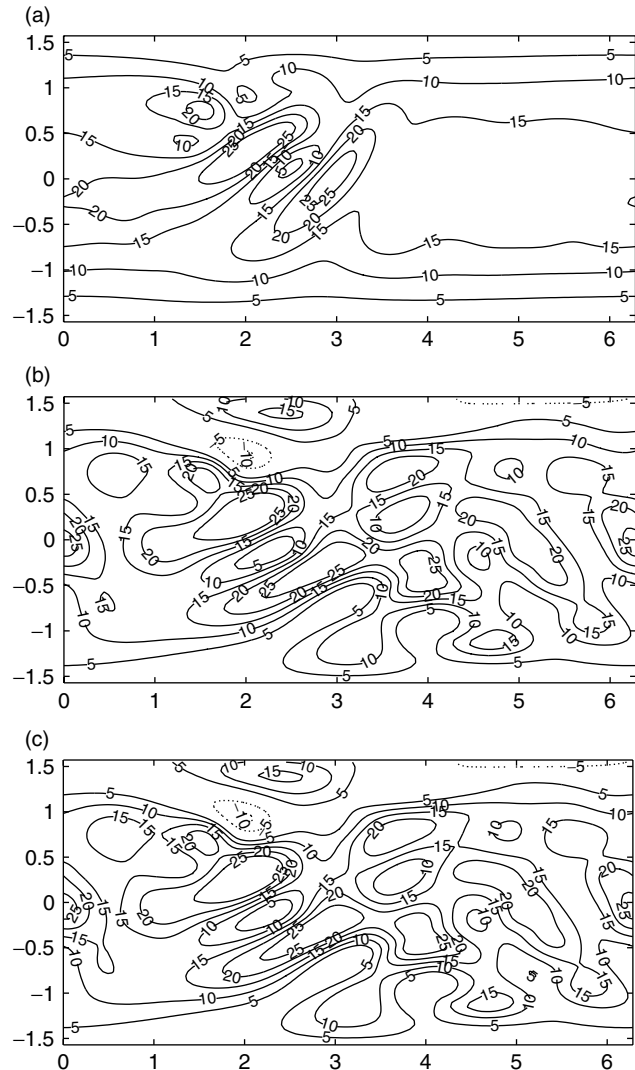
Figures 5(b), 6(b) and 7(b), respectively, show that their results and ours are very similar.

Also, for this test case, Nair *et al.* (2005) integrated their discontinuous Galerkin shallow-water model on a cubed sphere having 48×48 degrees of freedom per face. There are thus 192 degrees of freedom around the Equator compared to the 128 used in our integrations, so their resolution is approximately 50% finer than ours. Although not mentioned in their paper, they used a timestep of length $\Delta t = 90$ s (private communication). They reported that their integrations gave very similar results to the high-resolution spectral T213 results shown in Jakob-Chien *et al.* (1995), but without the spurious oscillations in the vicinity of the mountain associated (via Gibbs phenomenon) with its spectral representation. Comparison of Figures 4(b), (c) of Nair *et al.* (2005) with our Figures 5(a), (b), respectively, show that their results and ours are also very similar.
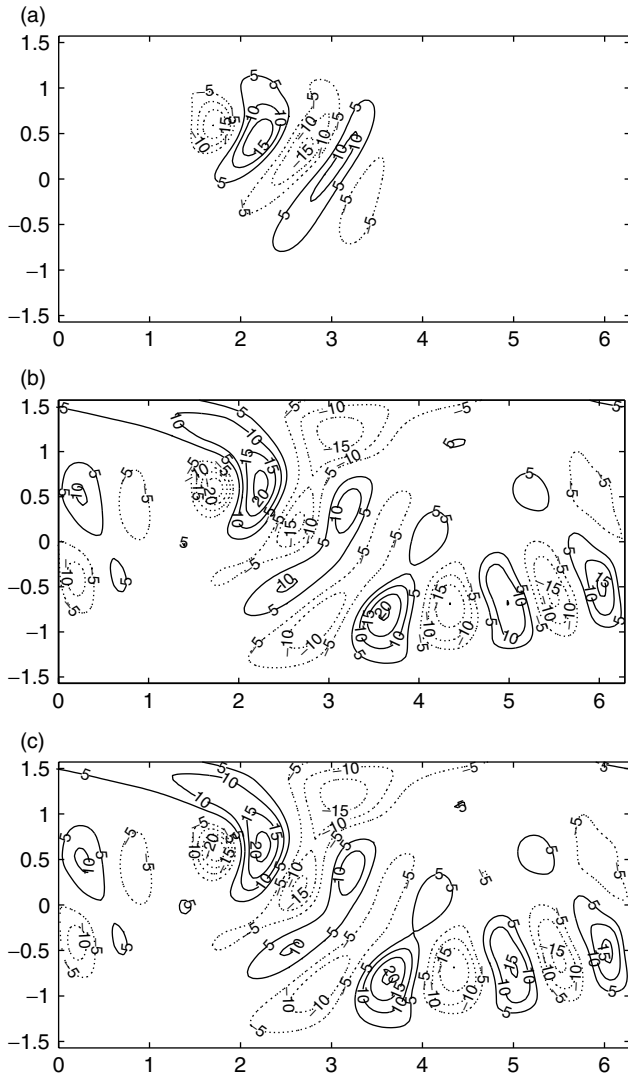
Figure 7. As Figure 6, but for the meridional wind component v.

Figure 8. Numerical solution after 15 days of integration using the standard SISL model with $\triangle t = 6000$ s for zonal flow over an isolated mountain on a 128×64 ($I \times J$) grid: (a) $(\Phi + \Phi^S)/g$ (m), (b) u, and (c) v. Contour intervals are 50 m for $(\Phi + \Phi^S)/g$, and $5\,\mathrm{m\,s^{-1}}$ for u and v. Solid lines denote positive contours, dashed lines negative contours, and there is no zero contour.

4. Conclusions

A mass-conserving SL discretisation (C-SLICE) of the continuity equation has been coupled to a SISL discretisation of the shallow-water momentum equations. The coupling is achieved in a straightforward way, analogous to how a standard SISL discretisation of the continuity equation is coupled to the momentum equations. In particular, and in contrast to the approach of Lauritzen *et al.* (2006) and Kaas (2008), it does not require the explicit evaluation of the Lagrangian divergence nor the use of any first-order departure point calculations.

In addition to exactly and inherently conserving mass, the discretisation has two further notable features. The first is that it follows the recommendations of TS04, in particular for the discrete form of the Coriolis terms, to give good Rossby mode dispersion properties and also to ensure that the Coriolis terms provide no source or sink of energy. The second is that the Cartesian transform approach of Wood *et al.* (2009) is used to calculate the departure points. An advantage of this is that the method is consistent with the matrix rotation method that
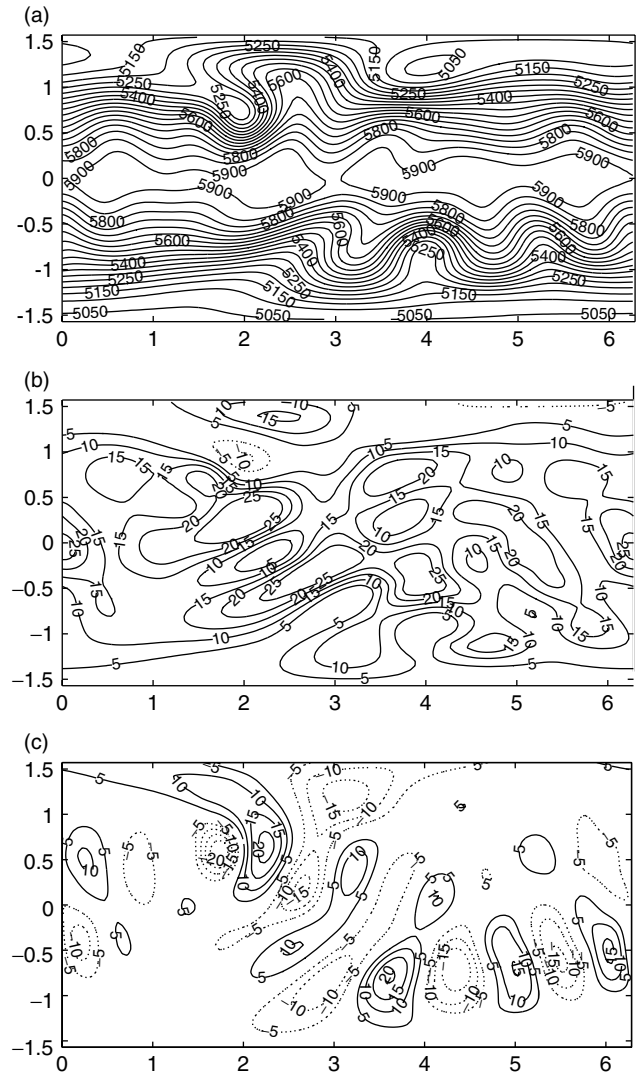
is applied to evaluate the components of the momentum equation (Staniforth *et al.*, 2009), thereby providing more coherency between the discrete forms of the kinematic and momentum equations.

A standard, non-mass-conserving SISL discretisation of the continuity equation has also been presented to provide a baseline against which to measure performance. Both the mass-conserving and non-conserving models have been applied to three published test problems: stationary jets over a zonal orography (Staniforth and White, 2007); exact unsteady flow (Läuter *et al.*, 2005, 2007); and zonal flow over an isolated mountain (Williamson *et al.*, 1992). The first two of these problems have analytic solutions and both models give good results, for a variety of spatial and temporal resolutions, as borne out by various error measures and plots of the differences with respect to the analytic solutions. Further, the mass-conserving scheme gives slightly better results than

the non-conserving scheme. This is ascribed to the use of a spline-based method for the conservative remapping of the mass-conserving scheme compared with cubic Lagrange interpolation for the non-conserving one. Similar results are also found for the Williamson *et al.* (1992) test case 5; when run with a timestep ($\Delta t = 6\,000$ s) that is an order of magnitude larger than is typically the case in the literature ($\Delta t = 600$ s), the results are almost indistinguishable from those obtained using the smaller timestep, which themselves are almost indistinguishable from similar results in the literature.

To obtain some indication of the overhead of using the conservative (SLICE) scheme to achieve inherent mass conservation, the mass-conserving and standard SISL models have been run on a single-processor workstation, with a limited, and similar, amount of code optimisation. It is found that the mass-conserving model is about 10% more expensive than the standard SISL one, confirming the expectation that this overhead is relatively modest.

Acknowledgements

Appendices

A. Rotation matrix

The appropriate rotation matrix for the shallow-water equations is the 2×2 shallow-atmosphere one given in section 3.2 of Staniforth *et al.* (2000). Thus

$$\Lambda \equiv \left[\begin{array}{cc} \Lambda_{11} & \Lambda_{12} \\ \Lambda_{21} & \Lambda_{22} \end{array} \right], \qquad (A.1)$$

where

$$\Lambda_{11} = \Lambda_{22} = \frac{Q_{11} + Q_{22}}{1 + Q_{33}}, \qquad \Lambda_{12} = -\Lambda_{21} = \frac{Q_{12} - Q_{21}}{1 + Q_{33}}, \qquad (A.2)$$

and

$$Q_{11} \equiv \cos(\lambda_A - \lambda_D), \qquad (A.3)$$
$$Q_{12} \equiv \sin\phi_D \sin(\lambda_A - \lambda_D), \qquad (A.4)$$
$$Q_{21} \equiv -\sin\phi_A \sin(\lambda_A - \lambda_D), \qquad (A.5)$$

$$Q_{22} \equiv \cos\phi_A \cos\phi_D + \sin\phi_A \sin\phi_D \cos(\lambda_A - \lambda_D), \qquad (A.6)$$

$$Q_{33} \equiv \sin\phi_A \sin\phi_D + \cos\phi_A \cos\phi_D \cos(\lambda_A - \lambda_D), \qquad (A.7)$$

are (selected) matrix elements of a 3×3 deep-atmosphere rotation matrix **Q**; Staniforth *et al.* (2009) provide further details.

B. Determination of departure points using a local Cartesian transform method

At each arrival point, define a local Cartesian coordinate system $Oxyz$, with its origin O at the centre of the sphere, and whose unit vectors $\mathbf{i}_c$, $\mathbf{j}_c$, $\mathbf{k}_c$ are parallel to the unit vectors $\mathbf{i}$, $\mathbf{j}$, $\mathbf{k}$ of the spherical coordinate system there. Let U and V be the components of the wind in the local Cartesian system corresponding to the components (u, v) in the spherical system, i.e.

$$\left(\begin{array}{c} U \\ V \end{array} \right) = \Lambda \left(\begin{array}{c} u \\ v \end{array} \right), \qquad (B.1)$$

where Λ is the rotation matrix defined in Appendix A. The departure point (X_D, Y_D) in the local system at the kth iteration is computed as:

$$X_D^{(k)} = -\gamma \Delta t \left[\alpha_x U_A^{n+1} + \beta_x U^n \left(\lambda_D^{(k-1)}, \phi_D^{(k-1)} \right) \right], \qquad (B.2)$$

$$Y_D^{(k)} = -\gamma \Delta t \left[\alpha_x V_A^{n+1} + \beta_x V^n \left(\lambda_D^{(k-1)}, \phi_D^{(k-1)} \right) \right], \qquad (B.3)$$

where $\gamma \equiv (1 + Q_{33})/2$; α_x is an off-centring parameter and $\beta_x \equiv 1 - \alpha_x$ ($\alpha_x = \beta_x = 1/2$ for all results presented here); $k = 1, 2$, i.e. only two iterations are used as they are sufficient for reasonable convergence (Staniforth and Côté, 1991). Conversion from (X_D, Y_D) to (λ_D, ϕ_D) is achieved using:

$$(\lambda_D - \lambda_A) = \tan^{-1} \left(\frac{X_D}{Z_D \cos\phi_A - Y_D \sin\phi_A} \right), \qquad (B.4)$$

$$\phi_D = \sin^{-1} \left(\frac{Y_D \cos\phi_A + Z_D \sin\phi_A}{\sqrt{X_D^2 + Y_D^2 + Z_D^2}} \right), \qquad (B.5)$$

where $Z_D^2 \equiv a^2 - X_D^2 - Y_D^2$ and the FORTRAN intrinsic function ATAN2 is employed in (B.4).

C. Difference and averaging operators

Let the domain

$$[\lambda_0, \lambda_I] \times [\phi_0, \phi_J] \equiv [0, 2\pi] \times \left[-\pi/2, +\pi/2 \right]$$

be divided into I intervals $[\lambda_{i-1}, \lambda_i]$, $i = 1, 2, \ldots, I$ in the λ direction, and J intervals $[\phi_{j-1}, \phi_j]$, $j = 1, 2, \ldots, J$ in the ϕ direction. u- v- and Φ-points are then located at $(\lambda_i, \phi_{j-1/2})$, $(\lambda_{i-1/2}, \phi_j)$ and $(\lambda_{i-1/2}, \phi_{j-1/2})$ respectively, where the half-integer coordinates are interleaved with the integer ones.

In what follows, the grid intervals are

$$\Delta\lambda_l \equiv \lambda_{l+\frac{1}{2}} - \lambda_{l-\frac{1}{2}}, \qquad \Delta\phi_l \equiv \phi_{l+\frac{1}{2}} - \phi_{l-\frac{1}{2}}, \qquad (C.1)$$

where the grid index l is a positive integral multiple of $1/2$.

Averaging operators $\overline{(\cdot)}^\lambda$, $\overline{(\cdot)}^\phi$, $\langle\cdot\rangle^\lambda$ and $\langle\cdot\rangle^\phi$ are defined via

$$\overline{F}^\lambda\Big|_{i,j} \equiv \left(\frac{\lambda_{i+\frac{1}{2}} - \lambda_i}{\Delta\lambda_i}\right)F_{i-\frac{1}{2},j} + \left(\frac{\lambda_i - \lambda_{i-\frac{1}{2}}}{\Delta\lambda_i}\right)F_{i+\frac{1}{2},j},$$
(C.2)

$$\overline{F}^\phi\Big|_{i,j} \equiv \left(\frac{\phi_{j+\frac{1}{2}} - \phi_j}{\Delta\phi_j}\right)F_{i,j-\frac{1}{2}} + \left(\frac{\phi_j - \phi_{j-\frac{1}{2}}}{\Delta\phi_j}\right)F_{i,j+\frac{1}{2}},$$
(C.3)

$$\langle F\rangle^\lambda\Big|_{i,j} \equiv \frac{1}{2}\left(F_{i-\frac{1}{2},j} + F_{i+\frac{1}{2},j}\right),$$
(C.4)

$$\langle F\rangle^\phi\Big|_{i,j} \equiv \frac{1}{2}\left(F_{i,j-\frac{1}{2}} + F_{i,j+\frac{1}{2}}\right),$$
(C.5)

where i and j are the horizontal grid indices in the λ and ϕ directions respectively. i and j are both positive, integral multiples of $1/2$. λ_i denotes the value of λ at the ith grid point in the λ-direction and ϕ_j denotes the value of ϕ at the jth grid point in the ϕ-direction. For a general variable, G, $G|_{i,j}$ denotes evaluation of G at the (i, j)th grid point.

Differencing operators δ_λ and δ_ϕ are defined via

$$(\delta_\lambda F)_{i,j} \equiv \frac{F_{i+\frac{1}{2},j} - F_{i-\frac{1}{2},j}}{\Delta\lambda_i},$$
$$(\delta_\phi F)_{i,j} \equiv \frac{F_{i,j+\frac{1}{2}} - F_{i,j-\frac{1}{2}}}{\Delta\phi_j}.$$
(C.6)

D. Algorithm for the iterative solution of the nonlinear coupled set of equations (27), (28) and (34)

Do $n = 1, N$ (time-step loop)
  – given the solution $(u, v, \Phi)^n$ at level n.
  Do $m = 1, M$ (outer-loop iteration, departure loop)
    – compute departure points using $(u, v)^n$ and the latest estimate for $(u, v)^{n+1}$.
    – evaluate $\left(R_u^n, R_v^n, R_\Phi^n\right)$ at departure points.
    Do $l = 1, L$ (inner-loop iteration, Coriolis loop)
      – evaluate $\left(R_u^*, R_v^*\right)$ and the right-hand side of (34).
      – solve the Helmholtz problem (34) for Φ^{n+1}.
      – update $(u, v)^{n+1}$ from (27)–(28).
    Enddo
  Enddo
Enddo

References

Durran DR, Reinecke PA. 2004. Instability in a class of explicit two-time-level semi-Lagrangian schemes. *Q. J. R. Meteorol. Soc.* **130**: 365–369.

Gravel S, Staniforth A. 1994. A mass conserving semi-Lagrangian scheme for the shallow-water equations. *Mon. Weather Rev.* **122**: 243–248.

Jakob-Chien R, Hack JJ, Williamson DL. 1995. Spectral transform solutions to the shallow-water test set. *J. Comput. Phys.* **119**: 164–187.

Kaas E. 2008. A simple and efficient locally mass conserving semi-Lagrangian transport scheme. *Tellus A* **60**: 305–320.

Lauritzen PH, Kaas E, Machenhauer B. 2006. A mass-conservative semi-implicit semi-Lagrangian limited-area shallow-water model on the sphere. *Mon. Weather Rev.* **134**: 1205–1221.

Lauritzen PH, Kaas E, Machenhauer B, Lindberg K. 2008. A mass-conservative version of the semi-implicit semi-Lagrangian HIRLAM. *Q. J. R. Meteorol. Soc.* **134**: 1583–1595.

Läuter M, Handorf D, Dethloff K. 2005. Unsteady analytical solutions of the spherical shallow-water equations. *J. Comput. Phys.* **210**: 535–553.

Läuter M, Handorf D, Rakowsky N, Behrens J, Frickenhaus S, Best M, Dethloff K, Hiller W. 2007. A parallel adaptive barotropic model of the atmosphere. *J. Comput. Phys.* **223**: 609–628.

Lin SJ, Rood RB. 1997. An explicit flux-form semi-Lagrangian shallow-water model on the sphere. *Q. J. R. Meteorol. Soc.* **123**: 2477–2498.

Machenhauer B, Olk M. 1997. The implementation of the semi-implicit cell-integrated semi-Lagrangian models. *Atmos.-Ocean* (special issue) **35**: 103–126.

Mahidjiba A, Qaddouri A, Côté J. 2008. Application of the Semi-Lagrangian Inherently Conserving and Efficient (SLICE) transport method to divergent flows on a C-grid. *Mon. Weather Rev.* **136**: 4850–4866.

Moorthi S, Higgins RW, Bates JR. 1995. A global multilevel atmospheric model using a vector semi-Lagrangian finite-difference scheme. Part II: Version with physics. *Mon. Weather Rev.* **123**: 1523–1541.

Nair R, Machenhauer B. 2002. The mass conservative cell-integrated semi-Lagrangian advection scheme on the sphere. *Mon. Weather Rev.* **130**: 649–667.

Nair R, Scroggs JS, Semazzi FHM. 2002. Efficient conservative global transport schemes for climate and atmospheric chemistry models. *Mon. Weather Rev.* **130**: 2059–2073.

Nair R, Scroggs JS, Semazzi FHM. 2003. A forward trajectory global semi-Lagrangian transport scheme. *J. Comput. Phys.* **190**: 275–294.

Nair RD, Thomas SJ, Loft RD. 2005. A discontinuous Galerkin global shallow water model. *Mon. Weather Rev.* **133**: 876–888.

Priestley A. 1993. A quasi-conservative version of the semi-Lagrangian advection scheme. *Mon. Weather Rev.* **121**: 621–629.

Rančić M. 1992. Semi-Lagrangian piecewise biparabolic scheme for two-dimensional horizontal advection of passive scalar. *Mon. Weather Rev.* **120**: 1394–1406.

Rančić M. 1995. An efficient conservative monotonic remapping for semi-Lagrangian transport algorithms. *Mon. Weather Rev.* **123**: 1213–1217.

Staniforth A, Côté J. 1991. Semi-Lagrangian integration schemes for atmospheric models – A review. *Mon. Weather Rev.* **119**: 2206–2223.

Staniforth A, Pudykiewicz J. 1985. Reply to comments on and addenda to 'Some properties and comparative performance of the semi-Lagrangian method of Robert in the solution of the advection-diffusion equation'. *Atmos.-Ocean* **23**: 195–200.

Staniforth A, White AA. 2007. Some exact solutions of geophysical fluid dynamics equations for testing models in spherical and plane geometry. *Q. J. R. Meteorol. Soc.* **133**: 1605–1614.

Staniforth A, White AA. 2008a. Stability of some exact solutions of the shallow-water equations for testing numerical models in spherical geometry. *Q. J. R. Meteorol. Soc.* **134**: 771–778.

Staniforth A, White AA. 2008b. Unsteady exact solutions of the flow equations for three-dimensional spherical atmospheres. *Q. J. R. Meteorol. Soc.* **134**: 1615–1626.

Staniforth A, White AA, Wood N. 2009. Rotation matrix treatment of vector equations in semi-Lagrangian models of the atmosphere. I: Momentum equation. *Q. J. R. Meteorol. Soc. submitted*.

Temperton C, Hortal M, Simmons A. 2001. A two-time-level semi-Lagrangian global spectral model. *Q. J. R. Meteorol. Soc.* **127**: 111–128.

Thuburn J. 2007. Rossby wave dispersion on the C-grid. *Atmos. Sci. Letts.* **8**: 37–42.

Thuburn J, Staniforth A. 2004. Conservation and linear Rossby-mode dispersion on the spherical C Grid. *Mon. Weather Rev.* **132**: 641–653.

White AA, Staniforth A. 2009. Stability criteria for shallow water flow above zonally symmetric orography on the sphere. *Q. J. R. Meteorol. Soc. submitted*.

Williamson DL. 2007. The evolution of dynamical cores for global atmospheric models. *J. Meteorol. Soc. Japan* **85B**: 241–269.

Williamson DL, Drake JB, Hack JJ, Jakob R, Swarztrauber PN. 1992. A standard test set for numerical approximations to the

shallow-water equations in spherical geometry. *J. Comput. Phys.* **102**: 211–224.

Wood N, White AA, Staniforth A. 2009. Rotation matrix treatment of vector equations in semi-Lagrangian models of the atmosphere. II: Kinematic equation. *Q. J. R. Meteorol. Soc. submitted.*

Zerroukat M, Wood N, Staniforth A. 2002. SLICE: A Semi-Lagrangian Inherently Conserving and Efficient scheme for transport problems. *Q. J. R. Meteorol. Soc.* **128**: 2801–2820.

Zerroukat M, Wood N, Staniforth A. 2004. SLICE-S: A Semi-Lagrangian Inherently Conserving and Efficient scheme for transport problems on the Sphere. *Q. J. R. Meteorol. Soc.* **130**: 2649–2664.

Zerroukat M, Wood N, Staniforth A. 2005. A monotonic and positive-definite filter for a Semi-Lagrangian Inherently Conserving and Efficient (SLICE) scheme. *Q. J. R. Meteorol. Soc.* **131**: 2923–2936.

Zerroukat M, Wood N, Staniforth A. 2006. The Parabolic Spline Method (PSM) for conservative transport problems. *Int. J. Numer. Meth. Fluid* **11**: 1297–1318.

Zerroukat M, Wood N, Staniforth A. 2007. Application of the Parabolic Spline Method (PSM) to a multi-dimensional conservative transport scheme (SLICE). *J. Comput. Phys.* **225**: 935–948.

Zerroukat M, Wood N, Staniforth A. 2009. An improved version of SLICE for conservative monotonic remapping on a C-grid. *Q. J. R. Meteorol. Soc.* **135**: 541–546.